Predicting operational windows of ELMs suppression by Resonant Magnetic Perturbations in the DIII-D and KSTAR tokamaks

Q.M. Hu[1], R. Nazikian[1], N.C. Logan[2], J.-K. Park[1], C. Paz-Soldan[3], S.M. Yang[1], B.A. Grierson[1], Y. In[4,5], Y.M. Jeon[4], M. Kim[4], S.K. Kim[6], D.M. Orlov[7], G.Y. Park[4], and Q. Yu[8]

[1] *Princeton Plasma Physics Laboratory, Princeton, NJ 08543-0451, USA*

[2] *Lawrence Livermore National Laboratory, 7000 East Ave, Livermore, CA 94550, USA*

[3] *Columbia University, 2960 Broadway, New York, NY 10027-6900, USA*

[4] *Korea Institute of Fusion Energy, Daejeon 34133, South Korea*

[5] *Ulsan National Institute of Science and Technology, Ulsan 44919, South Korea*

[6] *Princeton University, Princeton, NJ 08544, USA*

[7] *University of California, San Diego, California 92093-0417, USA*

[8] *Max-Plank-Institut fur Plasmaphysik, 85748 Garching, Germany*

E-mail: qhu@pppl.gov

Abstract

A newly developed plasma response model, combining the nonlinear two-fluid MHD code TM1 and toroidal MHD code GPEC run in ideal mode, quantitatively predicts the narrow isolated q_{95} windows ($\Delta q_{95}{\sim}0.1$) of ELM suppression by n = 1, 2 and 3 resonant magnetic perturbations (RMPs) in both DIII-D and KSTAR tokamaks across a wide range of plasma parameters. The key physics that unites both experimental observations and our simulations is the close alignment of essential resonant q-surfaces and the location of the top of the pedestal prior to an ELM. This alignment permits an applied RMP to produce field penetration due to the lower $\mathbf{E}\times\mathbf{B}$ rotation at the pedestal top rather than being screened. The model successfully predicts that narrow magnetic islands form when resonant field penetration occurs at the top of pedestal, and these islands are easily screened when q_{95} moves off resonance, leading to very narrow windows of ELM suppression (typically $\Delta q_{95}{\sim}0.1$). Furthermore, the observed reduction in the pedestal height is also well captured by the calculated classical collisional transport across the island. We recover observed q_{95}, β_N and plasma shape dependence of ELM suppression due to the effect of magnetic islands on pedestal transport and Peeling-Ballooning-Mode (PBM) stability. Importantly, experiments do occasionally observe wide windows of ELM suppression ($\Delta q_{95}{>}0.5$). Our model reveals that at low pedestal-top density multiple islands open, leading to wide operational windows of ELM suppression consistent with experiment. The model indicates that wide q_{95} windows of ELM suppression can be achieved at substantially higher pedestal pressure with less confinement degradation in DIII-D by operating at higher toroidal mode number (n = 4) RMPs. This can have significant implications for the operation of the ITER ELM control coils for maintaining high confinement together with ELM suppression.

I. INTRODUCTION

Effective control of the edge-localized modes (ELMs) is an essential issue for the operation of fusion devices such as ITER.[1,2] One method to control ELMs is with the use of resonant magnetic perturbations (RMPs),[3] which has been widely applied in tokamaks worldwide.[4–11] The successful full suppression of ELMs in DIII-D[3–5] led to the adoption of in-vessel ELM control coils for ITER,[2] and the subsequent success of ELM suppression on multiple devices[10–17] has increased the confidence to suppress ELMs in ITER. Recent work from DIII-D and elsewhere finds the constraints of access conditions for full ELM suppression by RMPs, including density, rotation, edge safety factor and plasma shape etc.[16,17] The mechanism determining these constraints needs to be addressed to strengthen the physics basis for predicting robust ELM suppression in ITER.

One common characteristic (or constraint) of ELM suppression by RMPs is the existence of well-separated narrow q_{95} windows ($\Delta q_{95} \approx 0.1$),[5] where q_{95} is the magnetic safety factor at 95% of the normalized poloidal magnetic flux. Full ELMs suppression is observed only at specific q_{95} ($q_{95}{\sim}m/n$) by RMPs with n = 2 and 3 in DIII-D,[5,14,17,18] n =1 and 2 in KSTAR,[15,19–22] n = 2 in ASDEX-Upgrade (AUG),[16] and n = 1, 2 and 3 in EAST.[11,23,24] Here, m and n are the poloidal and toroidal mode number. Experiments in AUG[16,25] and DIII-D[17] find that the change in the plasma shape requires a shift in the q_{95} to achieve ELM suppression. To operate at the narrow q_{95} windows of ELM suppression, a specific ratio of toroidal field and plasma current is required ($q_{95}{\sim}B_t/I_p$). Consequently, these narrow q_{95} windows lead to stringent conditions for ELM suppression and limitations on the operating flexibility. If only narrow q_{95} windows of ELM suppression can be achieved, then the ability to explore

burning plasma conditions in experimental rectors will be limited.

Along with demonstration of RMP-ELM suppression in tokamaks worldwide, the understanding of the underlying physical mechanisms responsible for ELM suppression as well as the q_{95} windows is also improving. The field line pitch angle resonant formation of a stochastic magnetic edge layer based on vacuum field calculation was proposed to interpret these q_{95} windows.[26–28,13,4,29–31] However, the highly nonlinear, rapidly flowing and highly conducting plasma in the pedestal are thought to effectively screen out resonant fields and prevent the formation of stochasticity.[27,32,33] While the kink-peeling response is found to be important in density pump-out and ELM suppression (MAST,[26,27,29] ASDEX-U[28,34] and DIII-D[13,35,36]), penetration of the applied RMPs on edge rational surfaces is a leading contender to explain the pedestal bifurcation into the ELM-suppressed state.[12,14,37] A paradigm, assuming RMP-driven magnetic island at the pedestal top stopped the buildup of the pedestal, was proposed based on linear 2D stability model to explain the q_{95} windows of ELM suppression.[37] Based on DIII-D experiments and linear two-fluid MHD modeling,[14] it has been speculated that the reason for the occurrence of q_{95} windows is the need for resonant surfaces with magnetic islands to be at certain radial positions near the pedestal top in order to prevent the expansion of the H-mode edge gradient region towards destabilization of ELMs. However, a resistive nonlinear two-fluid model incorporating plasma transport is required to capture the plasma response to RMP and unravel the q_{95} windows in the highly nonlinearly pedestal.[38]

Recent nonlinear two-fluid MHD simulations have shown that island formation at the top of the pedestal is quantitatively consistent with the onset of ELM suppression, while island formation at the foot of the pedestal is quantitatively consistent with density pump-out due to the enhanced parallel collisional transport across the islands.[39,40] These studies support the early hypothesis that magnetic islands at the pedestal top could prevent the onset of ELMs by preventing the expansion of the pedestal to an unstable width and hence remain stable to peeling-ballooning-mode (PBM).[37] The two-fluid simulations well-captured the fast-timescale (~ms) variations at the threshold of ELM suppression, including nonlinear bifurcations of the plasma flow, together with changes of the non-axisymmetric magnetic field structure observed in DIII-D.[12,13] In addition, the two-fluid model also revealed the dependence of pedestal-top penetration threshold on both density and rotation,[40] which qualitatively explained the access conditions of low density and high toroidal rotation observed in AUG[16] and DIII-D.[17] Further, recent nonlinear two-fluid analytical results also indicates the role of resonant field penetration at the pedestal top during ELM suppression.[41] These consistencies between the two-fluid MHD model and experiments enable quantitative understanding and prediction for the q_{95} windows of ELM suppression.

In a recent paper we showed that a quantitative description of the q_{95} dependence of ELM suppression on pedestal-top conditions is possible for DIII-D $n = 3$ RMP ELM suppression data using nonlinear two-fluid MHD modeling.[42] In our present work we extend the study to new DIII-D conditions and KSTAR to include the following: (1) RMP ELM suppression with toroidal mode number $n = 1, 2, 3$ and 4. (2) The dependence of the q_{95} ELM suppression windows on β_N and change in plasma shape in DIII-D, (3) strategies for achieving wide q_{95} ELM suppression windows including lowering the ELM suppression threshold or applying RMPs with higher toroidal mode number. This paper is structured as follows. First, in section II, a brief summary of the experimental database of $n = 2$ and 3 RMPs ELM suppression in the DIII-D tokamak, and $n = 1$ and 2 RMPs ELM suppression in the KSTAR tokamak are described. In section III.A, the nonlinear MHD model is introduced. Key features of q_{95} ELM suppression windows by $n = 3$ RMP from our recent paper[42] is highlighted in section III.B. In section III.C, the simulated q_{95} ELM suppression windows for $n = 1, 2$ and 3 are presented based on the DIII-D and KSTAR experiments. Section III.D discusses the experimental observations and MHD simulations of the effects of β_N and plasma shape on q_{95} windows of ELM suppression. Section III.E discusses expanding q_{95} windows of ELM suppression by lowering plasma density or applying RMP with high toroidal model number. A summary of results and discussion are given in section IV.

II. BASIC EXPERIMENTAL OBSERVATIONS

Controlling ELM crashes has been broadly investigated in both DIII-D and KSTAR tokamaks using RMPs with different toroidal mode numbers, and full ELM suppression can be accessed only in specific q_{95} windows.

The low-collisionality DIII-D discharges presented here are mainly configured in the ITER-similar-shape (ISS) with upper triangularity $\Delta_{up} \sim 0.3$ and lower triangularity $\Delta_{low} \sim 0.7$, as shown by the blue poloidal flux surfaces in Fig. 1(a). The major and minor radius are $R = 1.7$ m, $a = 0.6$ m, and the aspect-ratio $A = R/a = 2.83$. The in-vessel coils,[43] consisting of an upper row (IU) and lower row (IL), are configured in even-parity to generate either $n = 2$ or 3 RMPs with strong resonant coupling to the edge of rational surfaces. Using these $n = 2$ and 3 RMPs, ELMs control has been studied in ISS discharges with varying plasma parameters, i.e. neutral beam injected power ≈ 4-9 MW, normalized beta $\beta_N \approx 1.4$-2.5, normalized electron pedestal collisionality $\nu_e^* \approx 0.1$–0.5 and edge safety factor $q_{95} \approx 3.1$-4.5.

The KSTAR discharges presented here are configured at higher triangularity than ISS with upper triangularity $\Delta_{up} \sim 0.35$ and lower triangularity $\Delta_{low} \sim 0.85$, as shown by the poloidal cross section of poloidal flux surfaces in Fig. 1(b). The major and minor radius are $R = 1.8$ m, $a = 0.5$ m, and the aspect-ratio $A = R/a = 3.6$. The in-vessel-control-coil (IVCC) system,[44] consisting of top, middle and bottom rows as shown in Fig. 1(b), can be configured in +90 degree phasing[45] to generate either $n = 1$ or 2 RMPs with strong resonant coupling to the edge of rational surfaces. Using these $n = 1$ and 2 RMPs, KSTAR experiments have been devoted to control ELMs with

varying plasma parameters, i.e., neutral beam injected power $\approx$ 2-4.5 MW, normalized beta $\beta_N \approx$ 1.6-2.3, normalized electron pedestal collisionality $\nu_e^* \approx$ 0.1–1 and edge safety factor $q_{95} \approx$ 3.3-7.
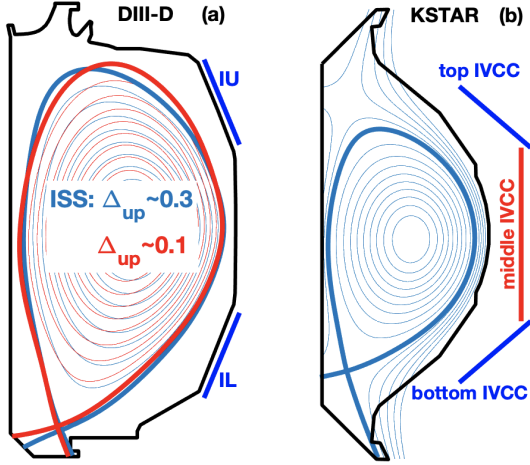

FIG. 1. Cross-sections of plasma shapes used in this study for (a) DIII-D tokamak with the location of upper I-coils (IU) and lower I-coils (IL), and (b) KSTAR tokamak with the location of top, middle and bottom in-vessel-control-coil (IVCC).

Fig. 2(a, b) shows the parameter space of complete ELM suppression versus q_{95} and pedestal density $n_{e,ped}$ observed in DIII-D using n = 3 and 2 RMPs, respectively. Here, each point indicates a single shot with constant q_{95} and complete ELM suppression sustained more than 200 ms, and q_{95} is from the magnetic equilibrium without bootstrap current effect. The plotted uncertainty in both q_{95} and $n_{e,ped}$ indicates their variation during ELM suppression. For n = 3 RMPs, ELM suppression can be accessed for $3.1 < q_{95} < 3.3$, $3.4 < q_{95} < 3.65$ and $3.8 < q_{95} < 4.0$ as shown in Fig. 2(a). A majority of ELM suppression discharges are achieved with $3.4 < q_{95} < 3.65$. Locking of core MHD modes and H-L transitions often occur at lower q_{95} ($q_{95} < 3.3$) when controlling ELM using n = 3 RMPs. On the other hand, the applied RMP strength is typically insufficient to suppress ELMs crash at higher q_{95} ($q_{95} > 3.8$). Fig. 2(a) also shows that the pedestal density is required to be lower than 3.5×10^{19} m^{-3} to achieve ELM suppression. This density threshold has been reported in both ASDEX-U[16] and DIII-D,[17] and it is interpreted by the dependence of pedestal-top penetration threshold on density according to nonlinear MHD modeling.[39,40] For n = 2 RMPs, ELM suppression has been achieved for $3.5 < q_{95} < 3.7$ and $4.05 < q_{95} < 4.25$ as shown in Fig. 2(b). Thus far, the density threshold for n = 2 RMP ELM suppression has been $n_{e,ped} < 3 \times 10^{19}$ m^{-3}.[46]

Fig. 2(c, d) shows the parameter space of complete ELM suppression versus q_{95} and edge density n_e observed in KSTAR using n = 1 and 2 RMPs, respectively. Here, each point indicates a single shot with constant or varying q_{95} and complete ELM suppression. The uncertainty in both q_{95} and $n_{e,ped}$ indicates their variation during ELM suppression. For n = 1 RMPs, ELM suppression can be accessed for $q_{95} \sim$ 4.1, 5.1

and 6.1 as shown in Fig. 2(c). A majority of ELM suppression discharges are achieved with $q_{95} \sim$ 5.1, since locking of core MHD modes and disruptions easily happen at lower q_{95} ($q_{95} < $ 4) when using n = 1 RMPs.[15,21] For n = 2 RMPs, ELM suppression has been achieved for $q_{95} \sim$ 3.3, 3.8, 4.3 and 4.8 as shown in Fig. 2(d).
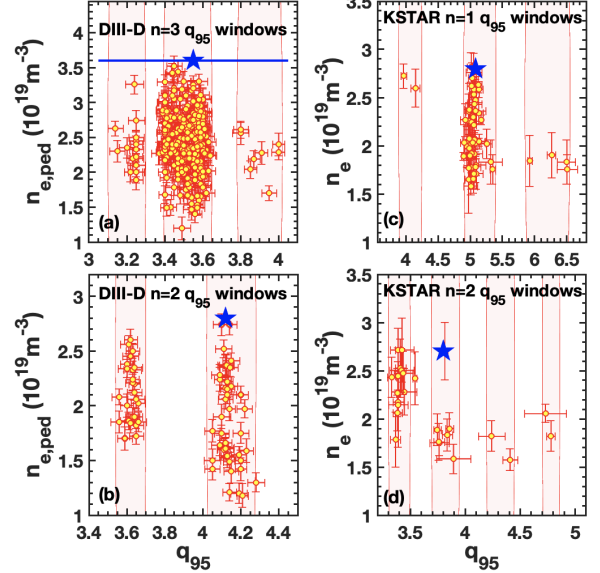

FIG. 2. Operating space of ELM suppression observed in (a,b) DIII-D with n = 3 and 2 RMPs and (c, d) KSTAR with n = 1 and 2 RMPs represented by the controlling variables of density and q_{95} from magnetic equilibrium, and the error bar indicates the variation of q_{95} and density during ELM suppression. Here, only ISS discharges are included in the DIII-D results. The edge line-averaged density is used for the KSTAR database. Here, the blue stars indicate the density and q_{95} of the target shots used in the TM1 simulations to predict the q_{95} windows and compare with these databases.

The observed q_{95} windows of ELM suppression in DIII-D and KSTAR contain discharges from many years' experiments, and usually the choice of q_{95} is based on empirical observations. In the following, nonlinear MHD modeling results are presented and compared with experimental results to quantitatively explain why there are narrow q_{95} windows of ELM suppression as observed in DIII-D and KSTAR. The blue stars in Fig. 2 indicate the density and q_{95} of the target shots used in TM1 simulations to predict the q_{95} windows of ELM suppression. The validation of the MHD modeling also enables further prediction and optimization of the access q_{95} of ELM suppression.

III. UNDERSTANDING OF q_{95} WINDOWS FOR ELM SUPPRESSION

A. The MHD model

For our analysis, we use a suite of codes to minimize the differences between the MHD model and experiment to obtain quantitative predictions of magnetic island formation at the top of pedestal of the DIII-D and KSTAR discharges: (1) the OMFIT framework[47] is used to consistently obtain the kinetic EFIT equilibrium and profiles of electron density, temperature

and $\mathbf{E} \times \mathbf{B}$ rotation frequency etc, based on experimental measurements. (2) The TM1 magnetic boundary condition is obtained from the toroidal ideal MHD plasma response calculations using the GPEC.[48] GPEC uses a kinetic equilibrium before ELM suppression to calculate the total (ideal plasma + vacuum field) response on the TM1 simulation boundary at $\psi_N = 1$, resolved into poloidal harmonics $\delta B_{m,n}$. Here, the ideal plasma response is mainly the edge kink (edge kink-peeling) response, which is thought to be important in ELM suppression.[13,34–36,49] (3) The TRANSP code[50] is used to infer the transport coefficients, including the momentum, particle and thermal diffusivities, from the measured profiles according to the calculations of power and particle balance. They are derived to be about ~1 m^2/s around the pedestal-top, and ~0.1 m^2/s in the steep gradient region. All three of these three are used by the nonlinear two-fluid MHD code TM1[51–53] to simulate the possible magnetic island formation and the associated transport.

TM1 is a nonlinear time-dependent two-fluid MHD code with cylindrical geometry and circular cross-section. TM1 includes the nonlinear coupling of harmonics of each helicity, and it solves the two-fluid MHD equations, including the generalized Ohm's law, the motion equation in the parallel and perpendicular direction, the continuity equation and the energy transport equation.[40,51–53] Specifically, it solves the motion equation by evaluating the torque balance between the electromagnetic ($\mathbf{J} \times \mathbf{B}$) torque due to the RMP and the plasma viscosity in the motion equation (see details in the Appendix of Ref. 40). Torque balance governs the bifurcation from screening to penetration of resonant fields in the pedestal, which is also sensitive to diamagnetic drifts through Ohm's law.[54] The electron density and temperature are self-consistently evaluated through the electron continuity equation and the energy transport equation. Physically, RMP enhances parallel collisional transport across the formed magnetic island or screening current, leading to enhanced particle and thermal transport across rational surfaces.[53,55,56] The temperature dependent neoclassical resistivity is utilized in the simulation to take into account the neoclassical effect in the toroidal geometry. The enhanced collisional particle and thermal transport are solved self-consistently with the penetration and/or screening of resonant fields in the TM1 code. Dedicated numerical methods are utilized in TM1 to reduce the numerical error associated with large values of the magnetic Reynolds number S and $\chi_\parallel/\chi_\perp$.[57] In addition, the radial grid size of 3200 is used to obtain high resolution simulation in the pedestal.

In tokamak experiments the plasma rotation is essentially toroidal, while in the TM1 model due to the large aspect ratio approximation only the poloidal rotation is included, so that an enhanced plasma viscosity (~100 times) for the $m/n = 0/0$ component is used in calculations. This value guarantees a reasonable balance between the electromagnetic and viscous force, based on the following considerations:[58] (a) The electromagnetic force in the toroidal direction is smaller by a factor $(n/m)(r_s/R)$ than that in the poloidal direction, where r_s is the minor radius of the resonant surface. (b) To have the same mode frequency due to the plasma rotation, the toroidal

rotation velocity should be (m/n) (R/r_s) times larger than the poloidal one. These two effects lead to a larger viscous force compared to the electromagnetic force for the toroidal rotation case by a factor $[(m/n)(R/r_s)]^2$, which is of the order of 10^2.

The cylindrical geometry utilized in the TM1 model is different from the toroidal strongly shaped geometry in the DIII-D and KSTAR experiments. The application of the full toroidal GPEC code includes the effects of shape and geometry in ideal plasma response,[13] which minimizes the discrepancy in the 3D magnetic boundary. Furthermore, in the nonlinear modeling, the small and separate magnetic island in the pedestal region causes a weak mode coupling effect arising from toroidal geometry.[40] Using experimental profiles and parameters, the combination of TM1 and GPEC consistently predicts the field penetration at the pedestal top and captures the most ubiquitous attributes and trends in the plasma response to RMPs in ELM suppression.[40] In the following, TM1 and GPEC are combined to predict magnetic island formation at the pedestal-top and its effect on pedestal pressure, which are correlated with the q_{95} windows of ELM suppression.

It is well known that the turbulence level is observed to increase following the application of RMPs[59,60] and transition to ELM suppression.[12] More recently XGC simulations claim that turbulence contributes to density pump-out,[61,62] but the simulations also show that the bulk of the pump-out arises from neoclassical transport across edge magnetic islands, which is consistent with the results from our nonlinear MHD model. According to our studies in Ref. 40, we are confident that the onset condition and parametric dependencies of ELM suppression and density pump-out is accounted for by the nonlinear MHD model without invoking turbulent transport. We take no account of such turbulence effects in this paper on transport, and we cannot say what role if any the ion-scale turbulence plays in these experiments.

B. Unraveling the q_{95} windows of n = 3 RMP ELM suppression

This section will highlight the characteristics of q_{95} windows for ELM suppression based on our previous work in Ref. 42. The modeling workflow was used to examine DIII-D ISS discharge with multiple q_{95} windows of ELM suppression caused by n = 3 RMPs, as shown in Fig. 3. The plasma parameters are as follows before applying RMPs: toroidal field $B_T = -1.9$ T, pedestal temperature $T_{e,ped} \approx 1$ keV, pedestal density $n_{e,ped} \approx 5.5 \times 10^{19}$ m^{-3}, beam power 7.3 MW, and neutral beam torque 6.7 Nm in the co-I_p direction. The ramping up plasma current from 1.3 MA to 1.65 MA results in q_{95} ramping downward from 4.1 to 3 as shown in Fig. 3(a). n = 3 RMPs are applied in even parity, and the constant coil current leads to complete ELM suppression in the separate q_{95} windows of $3.46 < q_{95} < 3.57$ (in t_b time window) and $3.18 < q_{95} < 3.31$ (in t_c time window) as indicated by the eliminated of D_α spikes in the yellow bands of Fig. 3(b). There is a third window of sparse ELMs (not fully suppressed) for $3.8 < q_{95} < 3.85$ (in t_a time window). RMPs cause strong density pump-out and confinement degradation, $n_{e,ped}$ decreased to 3.5×10^{19} m^{-3} (Fig.

3(c)), $P_{e,ped}$ decreased to 5.5 kPa (Fig. 3(d)). Both pedestal density and pressure are further decreased during ELM suppression as shown in the yellow bands of Fig. 3(c)-3(d). In detail, the pedestal pressure is decreased more than 15% during ELM suppression compared to the ELMing state. Fig. 3(d) also shows the EPED[37] prediction of $P_{e,ped}$ limited by PBM stability (red curve). The EPED model calculates the MHD stability limited height and width of the pedestal at each q_{95} value based on measurements of plasma parameters such as pedestal density, poloidal beta, shape, etc. The experimentally measured $P_{e,ped}$ is similar to the EPED prediction except at the q_{95} windows of ELM suppression. It should be pointed out that q_{95} from kinetic equilibrium is higher than that of magnetic equilibrium by ~0.1. For simplification, q_{95} from magnetic equilibrium is used hereafter for both experiment and simulation except when explicitly noted otherwise.
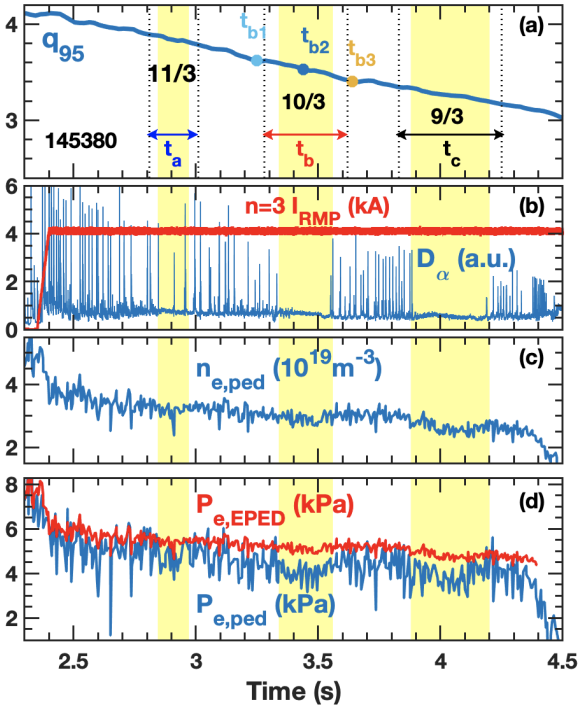

FIG. 3. Evolution of operational q_{95} windows scanning towards ELM suppression with constant RMPs coil current for discharge 145380, in terms of (a) q_{95}, (b) D_α signals and n = 3 I-coil current I_{RMP}, (c) pedestal density $n_{e,ped}$, and (d) measured (blue) and EPED predicted (red) pedestal pressure $P_{e,ped}$. The windows of ELM suppression are shaded in yellow.

The TM1 simulations for shot 145380 are introduced in detail in Figs. 2, 3 and 5 in Ref. 42. Here we briefly highlight the key features, which are critical for what follows. According to the simulations in Ref. 42, the q_{95} windows of ELM suppression coincide with the localization of narrow magnetic islands to the top of pedestal. In detail, it requires both that: (i) the imposed RMP strength is sufficient to form magnetic island at the pedestal top (Fig. 2 in Ref. 42), and (ii) the rational surface of the island is in the proper radial location to cause sufficient reduction in pedestal pressure (Fig. 2 in Ref.

42) and prevent further expanding for the pedestal to be unstable for PBMs (Fig. 3(a) in Ref. 42). Diagram in Fig. 4 summarize these features of Ref. 42. As illustrated in Fig. 4(a), RMP with the same strength forms magnetic island (with the width of $\Delta\psi_N \approx 0.016$) at the pedestal-top for q profiles at t_{b1} and t_{b2}, but it is shielded at t_{b3} profile as indicated by the saturated magnetic island width for m/n = 10/3 in circles. Here, the time slices t_{b1}, t_{b2} and t_{b3} are around the first full ELM suppression window t_b marked in Fig. 3(a). The 10/3 magnetic island at t_{b1} causes little reduction in the pedestal pressure (compared to the initial profile in black dotted curve from the experiment measurement before ELM suppression) because of both the more flattening pressure profile and the too far in rational surface compared to the location of the top of pedestal. The 10/3 magnetic island causes significant reduction in the pedestal pressure at t_{b2}, and it is consistent with experimental measurement as shown in magenta dotted curve in Fig. 4(a), although the flattening in the profile is not measured due to the limited spatial resolution of the diagnostic. Further comparison of pressure profile between TM1 simulation and experiment measurement are shown in Fig. 2(b) in Ref. 42. Since the plasma flow frequency at the rational surface is stronger at t_{b3} when the rational surface is too far out to the steep gradient region of the pedestal. Our MHD modeling in Ref. 42 confirmed the proposal working model from EPED.[37]
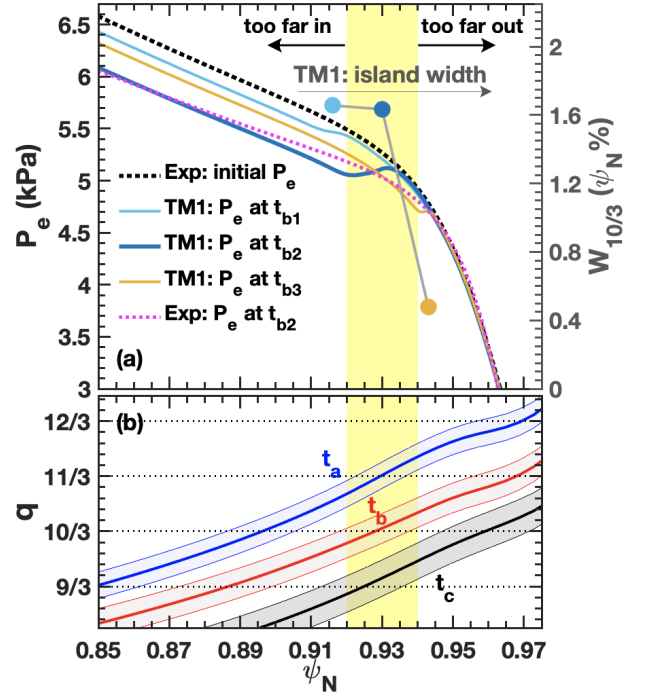

FIG. 4. Alignment between the locations of magnetic island and pedestal-top determines q_{95} windows of ELM suppression. Shown are (a) TM1 simulation of RMP effect on electron pressure P_e and the saturated island width (circles) for m/n = 10/3 at q profiles at t_{b1}, t_{b2} and t_{b3} with slightly different q_{95} (t_{b1}, t_{b2} and t_{b3} marked in Fig. 3(a)), (b) q profiles around time windows of t_a, t_b and t_c from Fig. 3(a) for discharge 145380. Here, the experimental measured pressure profile at t_{b2} is shown in magenta dotted in (a) for comparison.

The alignment between the locations of magnetic island and pedestal-top implies separate narrow q_{95} windows to access ELM suppression (Fig. 2 and 5 in Ref. 42). Figure 4(b) shows the profiles of q at the time windows of t_a, t_b to t_c marked in Fig. 3. To satisfy the pedestal-top alignment (in the yellow band), it requires a specific region of q_{95} for each resonant component, i.e. q_{95} ~11/3, 10/3, 9/3, etc as illustrated in Fig. 4(b). It is reasonable to expect such narrow q_{95} windows of ELM suppression for each resonant component, because of both the unaffected too far in magnetic island and strong flow frequency at too far out rational surface. Figure 5 shows the simulated boundary of q_{95} windows of ELM suppression for shot 145380 with 15% reduction in the pedestal pressure versus B_r and q_{95} in blue cures (details are discussed in Fig. 5(a) in Ref. 42). Depending on the RMP strength, the simulated q_{95} windows determined by 9/3 to 11/3 components are also qualitatively consistent with the DIII-D ELM suppression database by $n = 3$ RMP in Fig. 1(a), although there is larger scatter in this database. It should be noted that the q_{95} windows are predicted based on the single shot (145380), while $n_{e,ped}$ and β_N vary a lot for the database (Fig. 2(a)), which will lead to change in q_{95} windows as indicated by the scattering database in Fig. 5 and it will be further discussed in Sec. III.D.
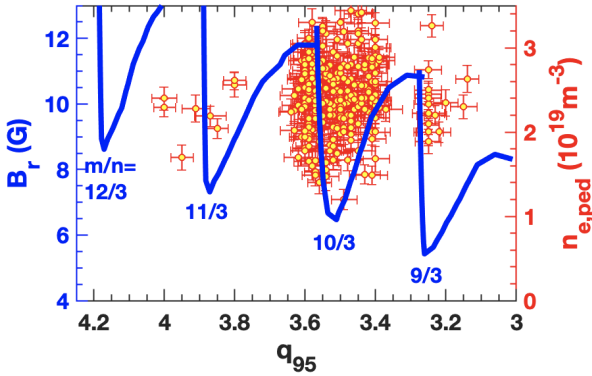

FIG. 5. Comparison between TM1 simulated boundary of q_{95} windows (blue curves) for discharge 145380 and DIII-D ELM suppression database by $n = 3$ RMP (red circles) from Fig. 2(a).

Figure 5 reveals that: (1) the width of q_{95} windows is sensitive to the applied RMP strength, relatively stronger RMPs suppress ELMs in a wider q_{95} window for the same resonant component. (2) The minimum threshold of RMP to access ELM suppression increases with increasing poloidal mode number (higher q_{95} as well). (3) Since the q_{95} windows are determined by discrete resonant components, the distance between neighboring q_{95} windows depends on the toroidal mode number of applied RMPs ~1/n, which is about Δq_{95} ~ 0.33 for $n = 3$ (Fig. 5). The many features of q_{95} ELM suppression windows raise a number of important issues for identifying which parameters affect the q_{95} windows, and whether this MHD model-based understanding can be widely validated from different devices. In the following, these issues will be further discussed.

C. q_{95} windows at different toroidal mode numbers

The modeling workflow is also used to predict the q_{95} windows of ELM suppression for RMP with different toroidal mode numbers in the DIII-D and KSTAR tokamaks. Figure 6 shows the simulated q_{95} windows of ELM suppression by $n = 2$ RMP represented by the pedestal pressure reduction versus q_{95} and RMP strength. The blue curves indicate the boundary with 15% reduction in the pedestal pressure. The profiles and plasma parameters are used from a low collisionality discharge 158115 at 3.25 s, q_{95} ~ 4.1 (the details of which are introduced in Ref. 40), and the q profile is shifted up and down to scan q_{95} from 3.3 to 4.8 in the simulation. Three q_{95} windows of ELM suppression are predicted, which are around q_{95} ~3.65, 4.15 and 4.65 determined by the $m/n = 7/2$, 8/2 and 9/2 resonant component RMPs. The $n = 2$ RMP ELM suppression windows in Fig. 6 show the similar features of the $n = 3$ windows shown in Fig. 5, but the distance between neighboring q_{95} windows is Δq_{95} ~ 0.5 for $n = 2$ RMP. In the DIII-D experiments, ELM suppression is observed with $3.5 < q_{95} < 3.7$ and $4.05 < q_{95} < 4.25$ (overlaid in red circles) due to the limited RMP strength, which is consistent with the predicted q_{95} windows determined by the 7/2 and 8/2 component RMPs in Fig. 6. According to the simulations, ELM suppression can be accessed with q_{95} ~ 3.15 determined by the 6/2 component, though core locked modes are easily triggered at such low q_{95}. For the experimental database, it is reasonable to observe a wider q_{95} window of 8/2 at lower density, since the pedestal density is lower than that of the target shot.
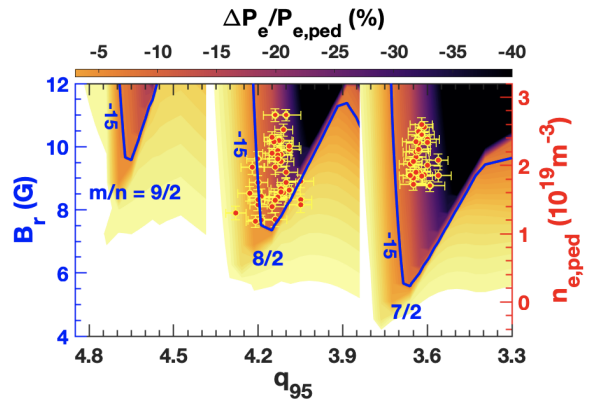

FIG. 6. TM1 simulated q_{95} windows of ELM suppression by $n = 2$ RMP for discharge 158115 in DIII-D represented by the contour plot of simulated relative reduction of pedestal pressure versus RMP strength B_r and q_{95}. The experimentally observed q_{95} regions are also overlaid by red circles versus q_{95} and $n_{e,ped}$.

Armed with the consistent prediction of q_{95} windows of ELM suppression for the DIII-D experiments, we proceed to predict the q_{95} windows for the KSTAR experiment when controlling ELMs by $n = 1$ and $n = 2$ RMPs. Figure 7 shows two target shots with RMP ELM suppression, shot 18730 (blue curves) with $n = 1$ RMP and shot 18594 (red curves) with $n = 2$ RMP, respectively. The triangularity of these two shots (Fig. 1(b)) is a bit different than the ISS. q_{95} ~ 5 for shot 18730, and the $n = 1$ RMP causes full ELM suppression at $t = 3.5$ s as shown in Fig. 7(b). While for shot 18594, q_{95} ~ 3.8,

and the slowly ramping-up $n = 2$ RMP causes full ELM suppression at $t = 12$ s as shown in Fig. 7(c). Both the applied $n = 1$ and 2 RMPs cause obvious density pump-out as indicated by the quick drop in the core line-averaged density in Fig. 7(d). Kinetic equilibrium and profiles at $t = 3.1$ s and 6.45 s for shots 18730 and 18594 are used for the MHD model to predict the q_{95} windows, respectively. The utilized $\mathbf{E}\times\mathbf{B}$ rotation frequency includes contribution from both the toroidal rotation and ion pressure gradient terms, while ignoring the poloidal rotation term which is not measured. According to neoclassical theory,[63] the contribution of poloidal rotation in the $\mathbf{E}\times\mathbf{B}$ rotation frequency may be similar to the magnitude of ion diamagnetic drift. This treatment may affect the predicted penetration threshold but will not significantly change the region of q_{95} to access ELM suppression. The profile of q is shifted up and down again to scan the q_{95} windows.

$m/n = 4/1$, 5/1 and 6/1 component islands formation at the pedestal top determine the ELM suppression windows at q_{95} around 4, 5 and 6. The q_{95} windows become wider when increasing RMP strength, and the distance between neighboring q_{95} windows is 1. This prediction is consistent with KSTAR experiments, as indicated by the comparison with its ELM suppression database in black circles, all these three q_{95} windows have been observed in the experiment.

The MHD model also correctly predicts the q_{95} windows for KSTAR $n = 2$ RMP ELM suppression as shown in Fig. 8(b). It shows the comparison between TM1 simulation based on shot 18594 and KSTAR $n = 2$ ELM suppression database. Six q_{95} windows determined by 6/2 to 11/2 component RMPs are predicted, and four of them are observed in the KSTAR experiments as indicated by the black circles, they are around 3.3, 3.8, 4.3 and 4.8. The scatter of the experimental database is probably due to the variation in the plasma parameters, for example the change in the pedestal density as shown in Fig. 2(d).
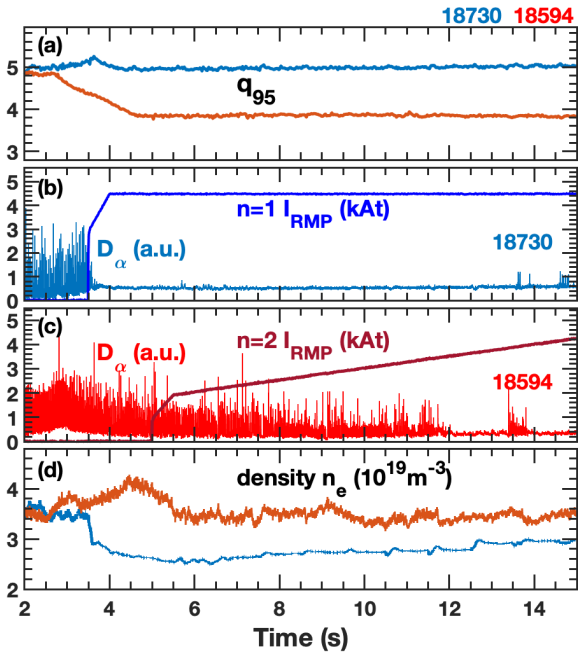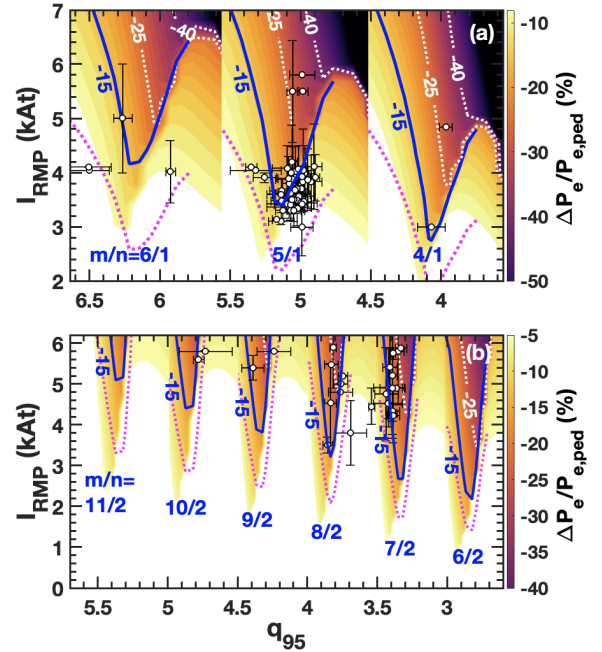

FIG. 7. ELM suppression by $n = 1$ RMPs at $q_{95} = 5$ (blue) and $n = 2$ RMPs at $q_{95} = 3.8$ (red) in the KSTAR tokamak. Shown are the time evolution of (a) q_{95}, (b) D_α signals and $n = 1$ RMP coil current, (c) D_α signals and $n = 2$ RMP coil current, and (d) core density for shots 18730 (blue) with $n = 1$ RMPs and 18594 (red) with $n = 2$ RMPs.

Based on the plasma parameters of shot 18730 and the q_{95} windows of ELM suppression for $n = 1$ RMP are predicted as shown in Fig. 8(a) represented by the pedestal pressure reduction versus q_{95} and RMP coil current. Due to missing pedestal profile measurements for some of the database, it is impossible to obtain kinetic EFIT and GPEC calculation for each discharge of the database. Here, the predicted RMP strength B_r is converted to RMP coil current utilizing the calculation with GPEC for the target shot 18730. This treatment enables direct comparison between TM1 prediction and the database by using the RMP coil current instead of B_r. The criterion of 15% reduction in pedestal pressure is also used, as indicated by the blue curves. It is predicted that the

FIG. 8. TM1 simulated q_{95} windows of ELM suppression by (a) $n = 1$ for discharge 18730 and (b) $n = 2$ RMP for discharge 18594 in KSTAR represented by the contour plot of simulated relative reduction of pedestal pressure versus RMP strength B_r and q_{95}. The magenta dotted curves in (a) and (b) indicate the expected ELM suppression boundary for the shot with the lowest density in the database. The experimentally observed q_{95} regions are also overlaid by black circles, and the errorbar indicates the variation of q_{95} and RMP coil current during complete ELM suppression. Here, the edge density of the target shots (18730 for $n = 1$, and 18594 for $n = 2$) is about 2.8×10^{19}m^{-3}, which is higher than that of most database shots.

The simulation results in Figs. 6 and 8 show agreement with DIII-D and KSTAR ELM control database, though q_{95} is scanned based on one single target shot. This agreement once again reveals that the close alignment of key resonant q-surfaces and the location of the top of the pedestal prior to an

ELM determines the q_{95} windows. This alignment permits an applied RMP to produce field penetration and prevent pedestal growth rather than being screened due to the lower $\mathbf{E} \times \mathbf{B}$ rotation at the pedestal top. It should be noted that results in Figs. 6 and 8 are each based on equilibrium and profiles of one single shot, the q_{95} windows of ELM suppression will differ slightly when the pedestal width is wider or narrower than that of the target shots. The effect of pedestal width on q_{95} windows will be introduced in the next section.

It should be noted that the q_{95} windows are predicted based on a single target shot for $n = 1$ (18730) and $n = 2$ (18594) RMP, respectively. The edge density of the target shot is higher than that of most database shots (Fig. 2(c, d)). When the pedestal density is lower (higher) than the target shot (Fig. 2(c, d)), the required RMP coil current will be lower (higher) than the predicted threshold.[40,42] For example, for those set of discharges with $q_{95} \sim 6.2$ in Fig. 8(a), the edge density is below 2×10^{19} m^{-3}, which is below the density of the target shot (3.3×10^{19} m^{-3} at $t = 3.1$ s in 18730) used in our analysis. From Eq. (2) in Ref. 40, for the shot with the lowest density in the database, we anticipate that the threshold RMP for ELM suppression will be 35% lower compared to the target shots as indicated by the magenta curves in Fig. 8(a, b). And the scattering database shots for the q_{95} windows of 6/1, 7/2 and 8/2 are almost within that boundary.
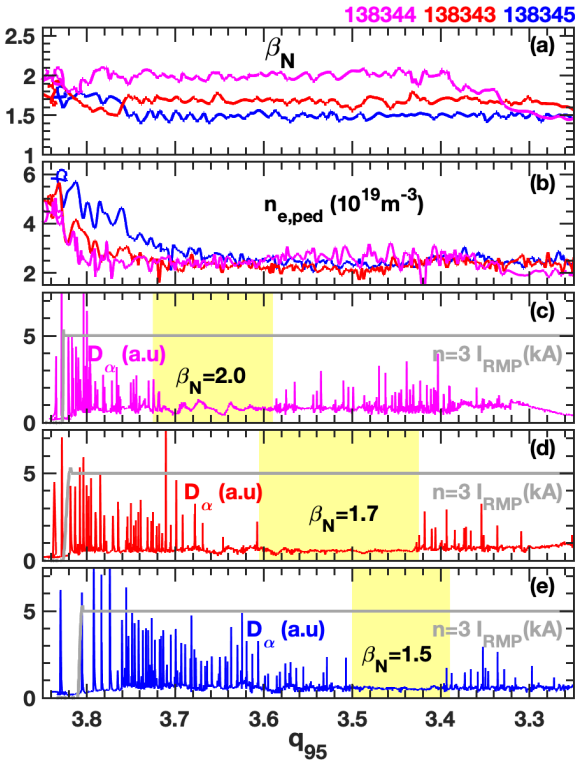

FIG. 9. Evolution of operational q_{95} windows scanning towards ELM suppression with constant $n = 3$ RMPs coil current and density but different β_N, in terms of (a) β_N, (b) pedestal density $n_{e,ped}$, D$_\alpha$ signals and $n = 3$ I-coil current for (c) shot 138344 (purple) with $\beta_N = 2.0$, (d) shot 138343 (red) with $\beta_N = 1.7$ and (e) shot 138345 (blue) with $\beta_N = 1.5$ versus q_{95}. The windows of ELM suppression are shaded in yellow.

D. β_N and shape effects

The requirement of close alignment of pedestal-top magnetic island formation indicates that the required q_{95} to access ELM suppression is sensitive to pedestal width. Experiments in DIII-D reveal β_N dependent q_{95} windows for ELM suppression by $n = 3$ RMP, as shown in Fig. 9. In the experiments, q_{95} is ramped downward from 3.9 to 3.2, the pedestal density is kept the same as shown in Fig. 9(b), while β_N is varied from 1.5 to 2 shot by shot as shown in Fig. 9(a). The applied $n = 3$ RMP with the same coil current (5 kA) leads to ELM suppression at different regions of q_{95}, i.e. $3.59 < q_{95} < 3.71$ for shot 138344 with $\beta_N = 2.0$ (Fig. 9(c)), $3.44 < q_{95} < 3.61$ for shot 138343 with $\beta_N = 1.7$ (Fig. 9(d)), and $3.39 < q_{95} < 3.51$ for shot 138345 with $\beta_N = 1.5$ (Fig. 9(e)). Obvious reduction in the pedestal pressure is also observed during the ELM suppression windows. There is a second q_{95} window of ELM suppression with $q_{95} < 3.3$ for shots 138343 and 138345, while H-mode confinement is terminated by a core locked mode when $q_{95} < 3.3$ for shot 138344. Figure 9 reveals that the access q_{95} for ELM suppression is mostly higher for higher β_N, which will be interpreted using the MHD model.
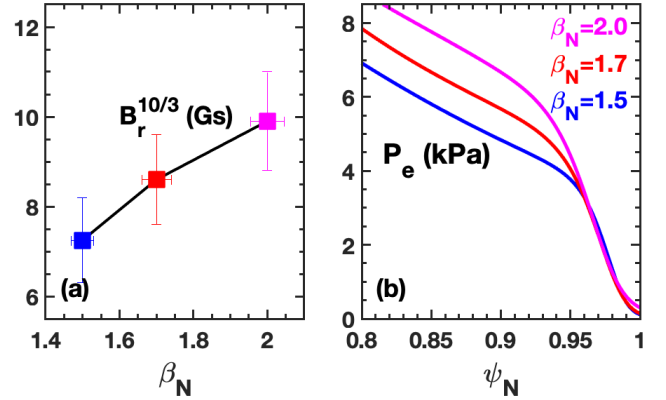

FIG. 10. Increasing β_N, leads to stronger magnetic response and wider pedestal, illustrated by (a) GPEC calculated B_r for the 10/3 component, and (b) the experimental profile of electron pressure P_e prior to ELM suppression at different β_N.

Figure 10(a) shows the GPEC calculated RMP strength of $m/n = 10/3$ resonant component at the plasma edge versus β_N using the kinetic equilibrium of these 3 shots just prior to ELM suppression. The errorbar in the results indicates the uncertainty due to slight variation in the equilibrium. Higher β_N leads to stronger plasma response, which is consistent with previous observations in DIII-D.[64–66] Stronger RMP is favorable for ELM suppression according to the simulations and scaling of pedestal-top penetration threshold.[40] The increasing β_N also correlates with increases in the pedestal width as shown in Fig. 10(b) represented by the electron pressure prior to the ELM suppression window measured by the Thomson scattering measurements.[67] The location of the top of the pedestal moves inward with the increasing pedestal width, which requires higher q_{95} to satisfy the requirement of the pedestal-top magnetic island alignment.

Simulations are performed to predict the q_{95} windows of ELM suppression for these three shots, and Fig. 11 shows the simulated boundary of 15% reduction in the pedestal pressure for the q_{95} window determined by the 10/3 resonant component. It shows that the q_{95} window shifts to higher q_{95} for higher β_N. The minimum threshold of RMP strength to access ELM suppression is stronger for higher β_N due to inner rational surface as well as lower resistivity, which increases the penetration threshold.[54] The shadowed regions indicate the q_{95} windows of ELM suppression for the applied RMP in these three shots, and the uncertainty of RMP strength is taken into account. It is found that the simulated q_{95} windows are consistent with the experimental observations as indicated by the black dotted lines, which correspond to the q_{95} windows of ELM suppression shown in Fig. 9. These results reveal that the wider pedestal together with the enhanced plasma response are responsible for the higher q_{95} window of ELM suppression when increasing β_N.
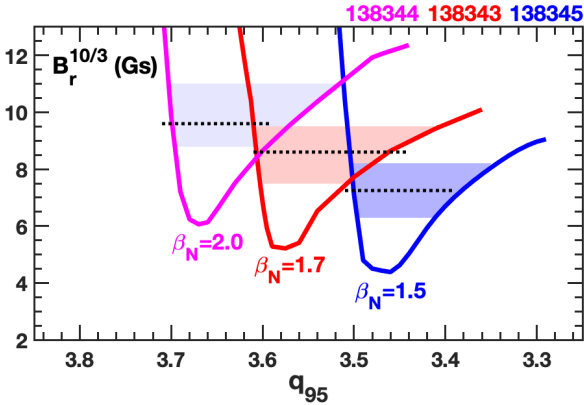

FIG. 11. TM1 simulated q_{95} windows of ELM suppression determined by m/n = 10/3 resonant component for shots 138344, 138343 and 138345 with different β_N. Shown is TM1 simulated boundary of 15% reduction in pedestal pressure caused by 10/3 RMP vs q_{95} and B_r. The black dotted lines indicate the observed q_{95} windows of ELM suppression shown in Fig. 9.

ELM suppression by RMPs is also observed to be sensitive to the shape of plasma, which has been reported in the DIII-D[17] and ASDEX-U tokamaks.[25] The pedestal width is understood to be dependent on plasma shape.[37,68] Both the pedestal height and width increase with triangularity, primarily due to an increase in the margin by which the edge pressure gradient exceeds the ideal ballooning mode first stability limit.[68]

The MHD model is used to understand the effect of plasma shape on q_{95} window of ELM suppression based on DIII-D observations.[17] Figure 12 shows two shots with ELM suppression by n = 3 RMP, shot 174712 (blue curves) with upper triangularity $\Delta_{up} \sim 0.3$ and shot 174689 (red curves) with $\Delta_{up} \sim 0.1$, respectively. The lower triangularity is the same $\Delta_{low} \sim 0.7$, and the detailed comparison of the plasma shape is shown in Fig. 1(a). In the experiment, the change in plasma shape impacts q_{95} though the plasma current is kept the same. The pedestal density is kept similar (Fig. 12(d)) and the same n =3 RMP coil current is applied. For shot 174712 with $\Delta_{up} \sim$

0.3, the favorable q_{95} is about 3.35 for robust full ELM suppression as shown in Fig. 12(a, b). While for shot 174689 with $\Delta_{up} \sim 0.1$, the favorable q_{95} is about 3.2 for ELM suppression as shown in Fig. 12(a, c). In contrast to shot 174712, shot 174689 appears to be marginal for full ELM suppression since ELMs appear at ~ 4.4 s.
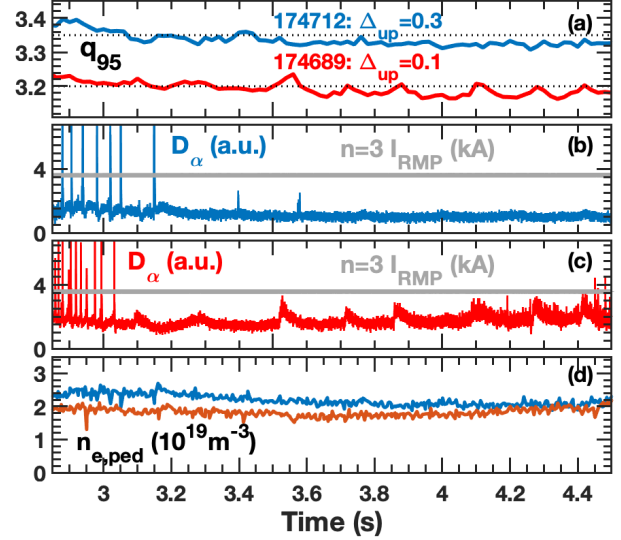

FIG. 12. ELM suppression by n = 3 RMPs at different q_{95} when varying the upper triangularity Δ_{up}. Shown are the time evolution of (a) q_{95}, (b, c) D_α signals and n = 3 RMP coil current, and (d) pedestal density $n_{e,ped}$ for shots 174712 (blue) with $\Delta_{up} \sim 0.3$ and 174689 (red) with $\Delta_{up} \sim 0.1$. Here, the plasma current is kept constant, but the change in plasma shape impacts q_{95}.
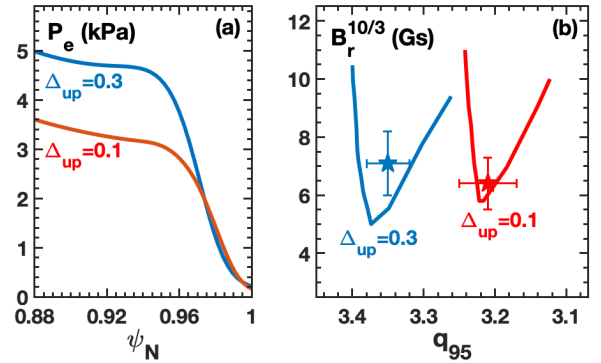

FIG. 13. Lower triangularity leads to narrower pedestal width, lower magnetic response and lower q_{95} for ELM suppression, illustrated by (a) the experimental profile of electron pressure P_e, and (b) TM1 simulated boundary of 15% reduction in pedestal pressure caused by 10/3 RMP vs q_{95} and B_r for $\Delta_{up} \sim 0.3$ (blue) and $\Delta_{up} \sim 0.1$ (red). Here, GPEC calculated RMP strength of 10/3 component is shown in stars in (b).

The measured electron pressure profile just prior to ELM suppression (at 2.9 s) shows higher and wider pedestal for shot 174712 ($\Delta_{up} \sim 0.3$) compared to shot 174689 ($\Delta_{up} \sim 0.1$) as shown in Fig. 13. It should be noted that the heating power for shot 174689 (5.8 MW) is 0.5 MW higher than shot 174712 (5.3 MW), while the pedestal electron temperature of shot 174712 is about 20% higher than shot 174689. The higher

pedestal height leads to stronger plasma response for shot 174712 as shown in Fig. 13(b) due to higher plasma beta at the top of the pedestal. Using the experimental parameters, the simulated boundary of 15% reduction in the pedestal pressure for the q_{95} window determined by the 10/3 resonant component is shown in Fig. 13(b). It shows a higher q_{95} window for $\Delta_{up} \sim 0.3$ (blue) compared to $\Delta_{up} \sim 0.1$ (red). According to the calculated RMP strength, it indicates that the applied RMP is enough to fully suppress ELMs in shot 174712 ($\Delta_{up} \sim 0.3$). While it is marginal for shot 174689 ($\Delta_{up} \sim 0.1$) where a slight change in the plasma conditions may cause a return to ELMing.

The experiments and simulation results in this section show that the change in β_N or triangularity essentially changes the pedestal height and width. This, in turn, changes the q_{95} windows for ELM suppression satisfying the alignment of pedestal-top magnetic islands. The change in the pedestal height will affect the plasma response, which will affect the width of q_{95} windows.

E. Expanding the q_{95} windows for ELM suppression

Simulations for both the DIII-D and KSTAR tokamaks indicate narrow q_{95} windows of ELM suppression for $n = 1, 2$ and 3 RMPs, and this will probably be the case in ITER. The specific narrow q_{95} windows for ELM suppression will limit the operational plasma current, as a result, it will challenge the operation flexibility of fusion devices when controlling ELMs. So, the question is: how can we expand the ELM suppression windows?

There are two ways to expand the q_{95} ELM suppression windows according to the simulation results: first, applying stronger RMP or decreasing the ELM suppression threshold. The simulated q_{95} windows reveal that stronger RMP will expand each q_{95} window and even make them merge together. According to the scaling the pedestal-top penetration threshold,[40] lowering the plasma density or the rotation frequency (by increasing toroidal rotation) will lower the ELM suppression threshold. As a result, each q_{95} window will also be expanded or even merged for the same RMP strength, although too large RMP may cause core locked modes.[15,20,21] Second, applying RMPs with higher toroidal mode number. Our simulations show that the distance between neighboring q_{95} windows is reversely proportional to the toroidal mode number, which is $\Delta q_{95} = 1/n$. The q_{95} windows are expected to be closer and easier to merge at high toroidal mode number. In the following, the first method is validated by DIII-D experiments, and prediction is presented for the second method.

Interestingly, experiments in DIII-D tokamak occasionally observed wider q_{95} windows of ELM suppression at lower density when applying $n = 3$ RMPs. Figure 14 shows the evolution of operational q_{95} windows scanning towards ELM suppression at different pedestal density, $n_{e,ped} \sim 2.5 \times 10^{19}$ m^{-3} for shot 132741 (blue) and $n_{e,ped} \sim 1.5 \times 10^{19}$ m^{-3} for shot 157303 (red). We have shown in Figs. 3 and 5 that at higher density ($n_{e,ped} \sim 3.5 \times 10^{19}$ m^{-3}), separate narrow 10/3 and 9/3 q_{95} windows can be accessed for full ELM suppression, while

it is marginal at the 11/3 window. At lower density for shot 132741, by applying the same RMP coil current, the two ELM suppression windows determined by 9/3 and 10/3 components windows expand and begin to merge into one ELM suppression window ($3.18 < q_{95} < 3.6$). Interestingly, the sparse ELMing window in Fig. 3 determined by the 11/3 component now becomes fully suppressed ($3.73 < q_{95} < 3.9$) in Fig. 14(b). When the density is further decreased to 1.5×10^{19} m^{-3} for shot 157303, one continuous ELM suppression window for $3 < q_{95} < 3.75$ is obtained due to the three windows merging together to form a much wider q_{95} window as shown in Fig. 14(c).
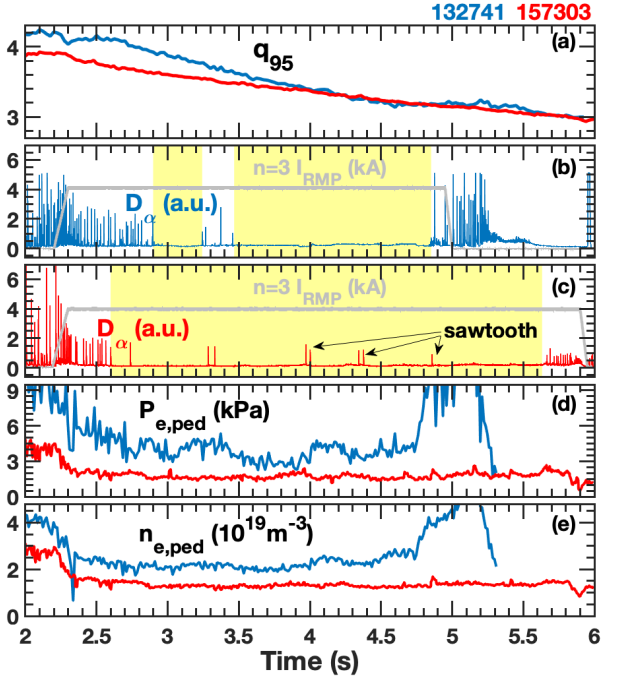

FIG. 14. Achieving wide operational q$_{95}$ windows of ELM suppression by lowering the density with constant RMPs coil current. Shown are time evolution of (a) q_{95}, (b,c) D$_\alpha$ signals and $n = 3$ I-coil current, (d) pedestal pressure $P_{e,ped}$, and (e) pedestal density $n_{e,ped}$ for shots 132741 (blue) and 157303 (red). The windows of ELM suppression are shaded in yellow.

Figure 15 shows the MHD simulations of shots 132741 and 157303. TM1 simulation for shot 132741 in Fig. 15(a) reproduces the oscillation in pedestal pressure and shows a consistent comparison with experiment and EPED prediction. Due to the lower density and higher pedestal rotation, the simulated pedestal pressure reduction in Fig. 15(b) reveals a lower RMP threshold to access the separate q_{95} windows for ELM suppression. For the experimental RMP strength (black dotted line), all the separate q_{95} windows become wider compared to shot 145380. Especially, the q_{95} windows determined by 10/3 and 9/3 components merge with each other, forming a wide continuous q_{95} window ($3 < q_{95} < 3.59$) of ELM suppression, which explains the observations in Fig. 14. Besides, the results in Fig. 15(b) show similar features of Fig. 5 except all the q_{95} windows are shifted slightly to lower q_{95} due to a slightly narrower pedestal in shot 132741.

Figure 15(c) shows the merging of all three q_{95} windows of ELM suppression, indicated by the sustained low pedestal pressure versus q_{95} in experiment, TM1 simulation and EPED prediction. The pedestal pressure no longer oscillates with q_{95} and stays well below the EPED prediction, due to the simultaneous appearance of multiple magnetic islands near the top of the pedestal, as shown in Fig. 16. Figure 15(d) shows the TM1 predicted reduction in the pedestal pressure versus q_{95} and RMP strength. The threshold of RMP strength to access the 15% reduction in pedestal pressure (blue curve) is substantially decreased due to the even lower density. The experimental RMP strength shown by the horizontal dashed line now intersects multiple overlapping ELM suppression windows. These overlapping windows near the pedestal top produce a continuous band of ELM suppression for $3 < q_{95} < 3.75$ as seen in Fig. 14.
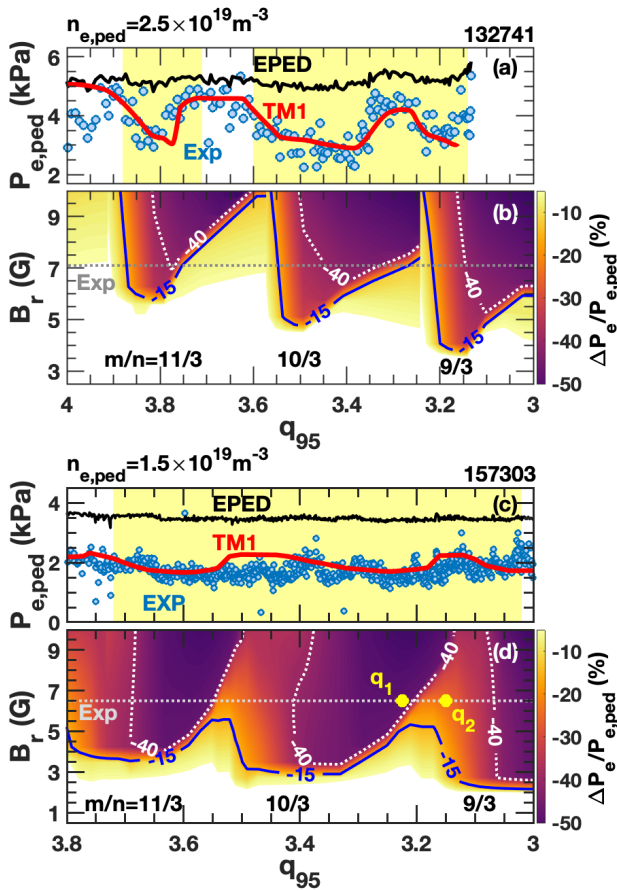

FIG. 15. TM1 simulated q_{95} windows of ELM suppression by $n = 3$ RMP for shots 132741 and157303: (a,c) comparison of pedestal pressure from experimental measurement (blue), EPED prediction (black) and TM1 simulation (red), and (b,d) the contour plot of simulated relative reduction of pedestal pressure versus RMP strength B_r and q_{95}. (Fig. 15(a,c) reproduced with permission from Phys. Rev. Lett. 125, 045001 (2020).[42] Copyright 2020 American Physical Society)

These ELM suppression windows now overlap at low density because the magnetic island at $q = 10/3$ is not fully screened before the adjacent island at $q = 9/3$ enters the top of the pedestal as q_{95} decreases. This produces a continuous band of ELM suppression, $3 < q_{95} < 3.75$, limited only by the range of the q_{95} scan. Figure 16(a) shows the Poincaré plot of the magnetic flux surfaces from TM1 simulation for $q_{95} = 3.225$ (q_1 marked in Fig. 15(d)) where the pedestal pressure reduction is largest. Two distinct islands appear near the pedestal top, one at $q = 10/3$ (most right island) and the other at $q = 9/3$. The top of pedestal electron pressure from TM1 is similar to experiment (red curve in Fig. 15(c)) and the TM1 electron pressure profile (white curve in Fig. 16(a)) is also similar to experiment (not shown here). For $q_{95} = 3.15$, the Poincaré plot in Fig. 16(b) shows the screening of the $m/n = 10/3$ island as it passes deeper into the gradient region of the pedestal, leaving just the $m/n = 9/3$ island at the top of the pedestal. It is important to highlight that even at the lowest pedestal density, the TM1 simulations show no significant magnetic stochasticity. Furthermore, resonant fields remain strong screening from $\psi_N = 0.96\text{-}0.98$, consistent with the preservation of the edge transport barrier.
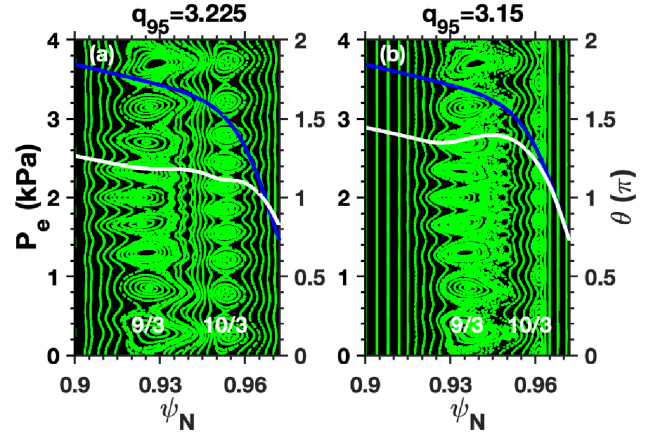

FIG. 16. Poincaré plot of the magnetic flux surfaces overlaid with the TM1 predicted pressure profile (white) and original pressure profile (blue) for (a) $q_{95} = 3.225$ and (b) $q_{95} = 3.15$ indicated in Fig. 16(d). (Fig. 16(a) reproduced with permission from Phys. Rev. Lett. 125, 045001 (2020).[42] Copyright 2020 American Physical Society)

A consequence of multiple islands near the pedestal top is that the pedestal pressure and width never recover between the ELM suppression windows, leading to a continuous q_{95} window of ELM suppression. Another consequence of multiple islands is that the pedestal pressure can fall well below the EPED model prediction, i.e. up to 50% reduction in pedestal pressure, which is not acceptable for high fusion power operation in ITER and future reactors. We are thus faced with the challenge of how to achieve wide windows of ELM suppression while optimizing the confinement. We see from Fig. 16 that expanded ELM suppression windows emerge when magnetic islands simultaneously form on adjacent rational surfaces near the top of the pedestal. When the rational surfaces are farther apart then the density (penetration) threshold must be lower for both islands to appear. This is because one of the islands must avoid getting screened in the steep gradient region of the pedestal. However, if the rational surfaces were to be closer to each other then the

density (penetration) threshold can be higher. The distance between the surfaces will decrease as we go to higher toroidal mode number.

In Ref. 42, we test this hypothesis using the plasma parameters of shot 145380 (high density discharge) and applying an $n = 4$ RMP in the simulations. Multiple ELM suppression windows are predicted for each resonance from $m/n = 16/4$ to $12/4$. For the same RMP amplitude as shot 145380, we predict potentially continuous windows of ELM suppression (merger of the 12/4, 13/4 and 14/4 ELM suppression windows), but now at high plasma density and causes just about 20% pressure reduction from the initial pedestal pressure. This is in contrast to $n = 3$ RMPs where there are no overlapping ELM suppression windows even for much larger RMP amplitudes (Fig. 3(b)). Therefore, the TM1 simulations predict that the closer proximity of adjacent rational surfaces at higher-n RMP allows multiple islands to appear at the pedestal top near the RMP threshold for field penetration, producing wide q_{95} windows of ELM suppression with weak pedestal pressure reduction. It should be noted, however, that higher-n RMPs impose higher current requirements for the same B_r as the plasma-coil distance increases.

These $n = 4$ calculations indicate that operationally favorable wide q_{95} ELM suppression windows may be achieved in DIII-D by operating at higher toroidal mode number. The newly planned M-coils[69] (12 coils) for DIII-D are designed to operate any of $n = 1$ to 6, which will enable exploring of this regime. By extension we also anticipate that operating ITER with dominant $n = 4$ RMPs could allow access to wider windows of ELM suppression relative to $n = 3$ operation. The currently planned ITER ELM control coils[2] can in principle operate with dominant $n = 4$ RMP but with some additional harmonics. In addition, equivalent to high-n RMP, RMPs with mixed toroidal mode number will also generate more components to resonate at the top of the pedestal to expand the q_{95} window. For example, $n = 2 + n = 3$, $n = 3 + n = 4$ and $n = 4 + n = 5$ etc are all available for the ITER ELM control coils, and the mixed $n = 2 + n = 3$ RMPs have been confirmed to reduce the ELM suppression threshold in DIII-D.[70]

IV. DISCUSSION AND CONCLUSION

The access conditions of q_{95} windows for ELM suppression by $n = 1$, 2 and 3 RMPs in both the DIII-D and KSTAR tokamaks are investigated in this paper using nonlinear two-fluid MHD equations with a cylindrical circular tokamak geometry. Due to the utilization of the full toroidal GPEC code, the difference between the cylindrical geometry utilized in the TM1 model and the toroidal strongly shaped geometry in the DIII-D and KSTAR experiments cause only a second-order effect in the pedestal region with strong flow shear. However, this second order effect may still lead to underestimate of the saturated width of the magnetic island, which can only be addressed by fully toroidal nonlinear simulations. We should note that the TM1 model does not

include the non-resonant plasma kink response, which is thought to, on the one hand, contribute 3D neoclassical effects on the particle transport.[48,71–73] Recent global gyrokinetic simulations with the XGC code do not show significant contribution of the kink response to neoclassical cross field transport for the low-collisionality plasmas.[61,62] On the other hand, the non-resonant 3D fields will strongly affect the plasma rotation through the neoclassical toroidal viscosity (NTV),[74–76] and the electron NTV was found to accelerate rotation and delay penetration threshold in KSTAR L-mode plasmas.[77] These effects will affect the penetration threshold and hence the ELM suppression threshold too. In addition, the experimental inputs to TM1 are taken after the initial pump-out and non-resonant braking, so they already implicitly take these into account. It is only the additional neoclassical transport from the island itself that the model neglects. Here, we do not claim that these effects are irrelevant for ELM suppression, but from the DIII-D low collisionality discharges we discussed in this paper, we do not see obvious changes in the toroidal rotation in the pedestal region except ELM suppression happened.

Our analysis reveals the importance of the close alignment of key resonant q-surfaces and the location of the top of the pedestal in determining the q_{95} windows. This alignment is relevant for the location of the top of the pedestal and the profile of safety factor q, which determines the correct resonant q-surfaces. ELM suppression depends on whether the applied RMP strength is higher than the suppression threshold. Therefore, the q_{95} windows of ELM suppression can be more accurately predicted compared to the ELM suppression threshold.

One may expect from our simulations that applying strong enough RMPs will always merge all the q_{95} windows to suppress ELMs no matter what q_{95} is. However, there are other limitations in the realistic experiments: first, strong enough RMP resonance at the steep gradient region of the pedestal will trigger a magnetic island. It has been reported that pedestal collapse occurs in DIII-D when the screening flow is inadequate to prevent field penetration by strong RMPs in the steep gradient region of the pedestal, and a subsequent H-L transition happens.[78] Second, strong enough RMP causes core locked modes and major disruptions.[79,80] Rotation deceleration caused by RMPs in the plasma core diminishes the stability of the core MHD and makes the plasma more susceptible to mode locking. The applied RMP can also directly drive and lock core tearing modes after ELM suppression, which is more likely to happen when applying RMP with low toroidal mode number as has been frequently observed in KSTAR.[15,20,21] These limitations will impose an upper threshold for the applied RMP strength. To avoid the above risks, it requires further optimization of the RMP spectrum to maximize those components responsible for ELM suppression but minimize other components responsible for pedestal collapse or core locked modes.[81]

In summary, a nonlinear MHD model predicts the ELM suppression conditions with good agreement in the DIII-D and KSTAR tokamaks for RMP with $n = 1$, 2 and 3. The key

physics that unites both experimental observations and our simulations is the close alignment of key resonant q-surfaces with the location of the top of the pedestal prior to an ELM. This alignment permits an applied RMP to produce field penetration that results in a significant drop in the pedestal width and pressure. The change in plasma beta or plasma shape also changes the pedestal width and height, and in turn affects both the ideal plasma kink-peeling response and q_{95} windows of ELM suppression. The simulation results suggest that raising the RMP strength or lowering the ELM by increasing the toroidal co-I_p rotation or decreasing density will expand the q_{95} windows, which is observed in DIII-D when applying $n = 3$ RMP. Finally, we predict wide q_{95} windows of ELM suppression for RMP with $n = 4$, which can be tested in future by DIII-D the M-coils and is accessible for ITER.

ACKNOWLEDGEMENTS

DISCLAIMER

DATA AVAILABILITY

The data that support the findings of this study are available from the corresponding author upon reasonable request.

REFERENCES

[1] A. Loarte, B. Lipschultz, A.S. Kukushkin, G.F. Matthews, P.C. Stangeby, N. Asakura, G.F. Counsell, G. Federici, A. Kallenbach, K. Krieger, A. Mahdavi, V. Philipps, D. Reiter, J. Roth, J. Strachan, D. Whyte, R. Doerner, T. Eich, W. Fundamenski, A. Herrmann, M. Fenstermacher, P. Ghendrih, M. Groth, A. Kirschner, S. Konoshima, B. LaBombard, P. Lang, A.W. Leonard, P. Monier-Garbet, R. Neu, H. Pacher, B. Pegourie, R.A. Pitts, S. Takamura, J. Terry, E. Tsitrone, and the ITPA Scrape-off Layer and Divertor Physics Topical Group, Nucl. Fusion **47**, S203 (2007).

[2] A. Loarte, G. Huijsmans, S. Futatani, L.R. Baylor, T.E. Evans, D.M. Orlov, O. Schmitz, M. Becoulet, P. Cahyna, Y. Gribov, A. Kavin, A.S. Naik, D.J. Campbell, T. Casper, E. Daly, H. Frerichs, A. Kischner, R. Laengner, S. Lisgo, R.A. Pitts, G. Saibene, and A. Wingen, Nucl. Fusion **54**, 033007 (2014).

[3] T.E. Evans, R.A. Moyer, P.R. Thomas, J.G. Watkins, T.H. Osborne, J.A. Boedo, E.J. Doyle, M.E. Fenstermacher, K.H. Finken, R.J. Groebner, M. Groth, J.H. Harris, R.J. La Haye, C.J. Lasnier, S. Masuzaki, N. Ohyabu, D.G. Pretty, T.L. Rhodes, H. Reimerdes, D.L. Rudakov, M.J. Schaffer, G. Wang, and L. Zeng, Phys. Rev. Lett. **92**, 235003 (2004).

[4] T.E. Evans, R.A. Moyer, K.H. Burrell, M.E. Fenstermacher, I. Joseph, A.W. Leonard, T.H. Osborne, G.D. Porter, M.J. Schaffer, P.B. Snyder, P.R. Thomas, J.G. Watkins, and W.P. West, Nat. Phys. **2**, 419 (2006).

[5] T.E. Evans, M.E. Fenstermacher, R.A. Moyer, T.H. Osborne, J.G. Watkins, P. Gohil, I. Joseph, M.J. Schaffer, L.R. Baylor, M. Bécoulet, J.A. Boedo, K.H. Burrell, J.S. deGrassie, K.H. Finken, T. Jernigan, M.W. Jakubowski, C.J. Lasnier, M. Lehnen, A.W. Leonard, J. Lonnroth, E. Nardon, V. Parail, O. Schmitz, B. Unterberg, and W.P. West, Nucl. Fusion **48**, 024002 (2008).

[6] Y. Liang, H.R. Koslowski, P.R. Thomas, E. Nardon, B. Alper, P. Andrew, Y. Andrew, G. Arnoux, Y. Baranov, M. Bécoulet, M. Beurskens, T. Biewer, M. Bigi, K. Crombe, E. De La Luna, P. de Vries, W. Fundamenski, S. Gerasimov, C. Giroud, M.P. Gryaznevich, N. Hawkes, S. Hotchin, D. Howell, S. Jachmich, V. Kiptily, L. Moreira, V. Parail, S.D. Pinches, E. Rachlew, and O. Zimmermann, Phys. Rev. Lett. **98**, 265004 (2007).

[7] A. Kirk, E. Nardon, R. Akers, M. Bécoulet, G.D. Temmerman, B. Dudson, B. Hnat, Y.Q. Liu, R. Martin, P. Tamain, D. Taylor, and the MAST team, Nucl. Fusion **50**, 034008 (2010).

[8] J.M. Canik, T.E. Evans, R.E. Bell, S.P. Gerhardt, B.P. LeBlanc, J. Manickam, J.E. Menard, T.H. Osborne, J.-K. Park, S.F. Paul, P.B. Snyder, S.A. Sabbagh, H.W. Kugel, E.A. Unterberg, and the NSTX Team, Phys. Rev. Lett. **104**, 045001 (2010).

[9] W. Suttrop, T. Eich, J.C. Fuchs, S. Günter, A. Janzer, A. Herrmann, A. Kallenbach, P.T. Lang, T. Lunt, M. Maraschek, R.M. McDermott, A. Mlynek, T. Pütterich, M. Rott, T. Vierle, E. Wolfrum, Q. Yu, I. Zammuto, and H. Zohm, Phys. Rev. Lett. **106**, 225004 (2011).

[10] Y.M. Jeon, J.-K. Park, S.W. Yoon, W.H. Ko, S.G. Lee, K.D. Lee, G.S. Yun, Y.U. Nam, W.C. Kim, J.-G. Kwak, K.S. Lee, H.K. Kim, and H.L. Yang, Phys. Rev. Lett. **109**, 035004 (2012).

[11] Y. Sun, Y. Liang, Y.Q. Liu, S. Gu, X. Yang, W. Guo, T. Shi, M. Jia, L. Wang, B. Lyu, C. Zhou, A. Liu, Q. Zang, H. Liu, N. Chu, H.H. Wang, T. Zhang, J. Qian, L. Xu, K. He, D. Chen, B. Shen, X. Gong, X. Ji, S. Wang, M. Qi, Y. Song, Q. Yuan, Z. Sheng, G. Gao, P. Fu, and B. Wan, Phys. Rev. Lett. **117**, 115001 (2016).

[12] R. Nazikian, C. Paz-Soldan, J.D. Callen, J.S. deGrassie, D. Eldon, T.E. Evans, N.M. Ferraro, B.A. Grierson, R.J. Groebner, S.R. Haskey, C.C. Hegna, J.D. King, N.C. Logan, G.R. McKee, R.A. Moyer, M. Okabayashi, D.M. Orlov, T.H. Osborne, J.-K. Park, T.L. Rhodes, M.W. Shafer, P.B. Snyder, W.M. Solomon, E.J. Strait, and M.R. Wade, Phys. Rev. Lett. **114**, 105002 (2015).

[13] C. Paz-Soldan, R. Nazikian, S.R. Haskey, N.C. Logan, E.J. Strait, N.M. Ferraro, J.M. Hanson, J.D. King, M.J. Lanctot, R.A. Moyer, M. Okabayashi, J.-K. Park, M.W. Shafer, and B.J. Tobias, Phys. Rev. Lett. **114**, 105001 (2015).

[14] M.R. Wade, R. Nazikian, J.S. deGrassie, T.E. Evans, N.M. Ferraro, R.A. Moyer, D.M. Orlov, R.J. Buttery, M.E. Fenstermacher, A.M. Garofalo, M.A. Lanctot, G.R. McKee, T.H. Osborne, M.A. Shafer, W.M. Solomon, P.B. Snyder, W. Suttrop, A. Wingen, E.A. Unterberg, and L. Zeng, Nucl. Fusion **55**, 023002 (2015).

[15] J.-K. Park, Y. Jeon, Y. In, J.-W. Ahn, R. Nazikian, G. Park, J. Kim, H. Lee, W. Ko, H.-S. Kim, N.C. Logan, Z. Wang, E.A. Feibush, J.E. Menard, and M.C. Zarnstroff, Nat. Phys. **14**, 1223 (2018).

[16] W. Suttrop, A. Kirk, V. Bobkov, M. Cavedon, M. Dunne, R.M. McDermott, H. Meyer, R. Nazikian, C. Paz-Soldan, D.A. Ryan, E. Viezzer, M. Willensdorfer, and the ASDEX Upgrade and MST Teams, Nucl. Fusion **58**, 096031 (2018).

[17] C. Paz-Soldan, R. Nazikian, L. Cui, B.C. Lyons, D.M. Orlov, A. Kirk, N.C. Logan, T.H. Osborne, W. Suttrop, and D.B. Weisberg, Nucl. Fusion **59**, 056012 (2019).

[18] M.J. Lanctot, R.J. Buttery, J.S. de Grassie, T.E. Evans, N.M. Ferraro, J.M. Hanson, S.R. Haskey, R.A. Moyer, R. Nazikian, T.H. Osborne, D.M. Orlov, P.B. Snyder, M.R. Wade, and the DIII-D Team, Nucl. Fusion **53**, 083019 (2013).

[19] Y. In, J.-K. Park, Y.M. Jeon, J. Kim, G.Y. Park, J.-W. Ahn, A. Loarte, W.H. Ko, H.H. Lee, J.W. Yoo, J.W. Juhn, S.W. Yoon, H. Park, and 3D Physics Task Force in KSTAR, Nucl. Fusion **57**, 116054 (2017).

[20] Y. In, A. Loarte, H.H. Lee, K. Kim, Y.M. Jeon, J.-K. Park, J.-W. Ahn, G.Y. Park, M. Kim, H. Park, and the 3D Physics Task Force in KSTAR, Nucl. Fusion **59**, 126045 (2019).

[21] Y. In, Y.M. Jeon, J.-K. Park, A. Loarte, J.-W. Ahn, J.H. Lee, H.H. Lee, G.Y. Park, K. Kim, H.S. Kim, W.H. Ko, T. Rhee, J. Kim, S.W. Yoon, H. Park, and the 3D Physics Task Force in KSTAR, Nucl. Fusion **59**, 056009 (2019).

[22] M. Kim, J. Lee, W.H. Ko, S.-H. Hahn, Y. In, Y.M. Jeon, W. Suttrop, S.K. Kim, G.Y. Park, J.-W. Juhn, and J.H. Lee, Phys. Plasmas **27**, 112501 (2020).

[23] Y. Sun, M. Jia, Q. Zang, L. Wang, Y. Liang, Y.Q. Liu, X. Yang, W. Guo, S. Gu, Y. Li, B. Lyu, H. Zhao, Y. Liu, T. Zhang, G. Li, J. Qian, L. Xu, N. Chu, H.H. Wang, T. Shi, K. He, D. Chen, B. Shen, X. Gong, X. Ji, S. Wang, M. Qi, Q. Yuan, Z. Sheng, G. Gao, Y. Song, P. Fu, B. Wan, and EAST Contributors, Nucl. Fusion **57**, 036007 (2017).

[24] S. Gu, B. Wan, Y. Sun, N. Chu, Y.Q. Liu, T. Shi, H.H. Wang, M. Jia, and K. He, Nucl. Fusion **59**, 126042 (2019).

[25] W. Suttrop, A. Kirk, R. Nazikian, N. Leuthold, E. Strumberger, M. Willensdorfer, M. Cavedon, M. Dunne, R. Fischer, S. Fietz, J.C. Fuchs, Y.Q. Liu, R.M. McDermott, F. Orain, D.A. Ryan, E. Viezzer, and The ASDEX Upgrade Team, The DIII-D Team and The Eurofusion MST Team, Plasma Phys. Control. Fusion **59**, 014049 (2016).

[26] A. Kirk, Y. Liu, E. Nardon, P. Tamain, P. Cahyna, I. Chapman, P. Denner, H. Meyer, S. Mordijck, and the MAST team, Plasma Phys. Control. Fusion **53**, 065011 (2011).

[27] Y. Liu, A. Kirk, Y. Gribov, M.P. Gryaznevich, T.C. Hender, and E. Nardon, Nucl. Fusion **51**, 083002 (2011).

[28] D.A. Ryan, Y.Q. Liu, A. Kirk, W. Suttrop, B. Dudson, M. Dunne, R. Fischer, J.C. Fuchs, M. Garcia-Munoz, B. Kurzan, P. Piovesan, M. Reinke, M. Willensdorfer, and the ASDEX-Upgrade team and the MST team, Plasma Phys. Control. Fusion **57**, 095008 (2015).

[29] Y. Liu, C.J. Ham, A. Kirk, L. Li, A. Loarte, D.A. Ryan, Y. Sun, W. Suttrop, X. Yang, and L. Zhou, Plasma Phys. Control. Fusion **58**, 114005 (2016).

[30] O. Schmitz, T.E. Evans, M.E. Fenstermacher, E.A. Unterberg, M.E. Austin, B.D. Bray, N.H. Brooks, H. Frerichs, M. Groth, M.W. Jakubowski, C.J. Lasnier, M. Lehnen, A.W. Leonard, S. Mordijck, R.A. Moyer, T.H. Osborne, D. Reiter, U. Samm, M.J. Schaffer, B. Unterberg, W.P. West, and the DIII-D and TEXTOR Research Teams, Phys. Rev. Lett. **103**, 165005 (2009).

[31] O. Schmitz, T.E. Evans, M.E. Fenstermacher, M. Lehnen, H. Stoschus, E.A. Unterberg, J.W. Coenen, H. Frerichs, M.W. Jakubowski, R. Laengner, C.L. Lasnier, S. Mordijck, R.A. Moyer, T.H. Osborne, H. Reimerdes, D. Reiter, U. Samm, B. Unterberg, and the DIII-D and TEXTOR teams, Nucl. Fusion **52**, 043005 (2012).

[32] N.M. Ferraro, Phys. Plasmas **19**, 056105 (2012).

[33] M. Becoulet, F. Orain, P. Maget, N. Mellet, X. Garbet, E. Nardon, G.T.A. Huysmans, T. Casper, A. Loarte, P. Cahyna, A. Smolyakov, F.L. Waelbroeck, M. Schaffer, T. Evans, Y. Liang, O. Schmitz, M. Beurskens, V. Rozhansky, and E. Kaveeva, Nucl. Fusion **52**, 054003 (2012).

[34] D.A. Ryan, Y.Q. Liu, A. Kirk, W. Suttrop, B. Dudson, M. Dunne, M. Willensdorfer, and the ASDEX Upgrade Team, The DIII-D Team and The Eurofusion MST Team, Plasma Phys. Control. Fusion **60**, 065005 (2018).

[35] N.C. Logan, L. Cui, H. Wang, Y. Sun, S. Gu, G. Li, R. Nazikian, and C. Paz-Soldan, Nucl. Fusion **58**, 076016 (2018).

[36] N.C. Logan, C. Paz-Soldan, J.-K. Park, and R. Nazikian, Phys. Plasmas **23**, 056110 (2016).

[37] P.B. Snyder, T.H. Osborne, K.H. Burrell, R.J. Groebner, A.W. Leonard, R. Nazikian, D.M. Orlov, O. Schmitz, M.R. Wade, and H.R. Wilson, Phys. Plasmas **19**, 056115 (2012).

[38] R. Fitzpatrick, Phys. Plasmas **25**, 112505 (2018).

[39] Q.M. Hu, R. Nazikian, B.A. Grierson, N.C. Logan, J.-K. Park, C. Paz-Soldan, and Q. Yu, Phys. Plasmas **26**, 120702 (2019).

[40] Q.M. Hu, R. Nazikian, B.A. Grierson, N.C. Logan, C. Paz-Soldan, and Q. Yu, Nucl. Fusion **60**, 076001 (2020).

[41] R. Fitzpatrick, Phys. Plasmas **27**, 042506 (2020).

[42] Q.M. Hu, R. Nazikian, B.A. Grierson, N.C. Logan, D.M. Orlov, C. Paz-Soldan, and Q. Yu, Phys. Rev. Lett. **125**, 045001 (2020).

[43] T.E. Evans, K.H. Burrell, M.E. Fenstermacher, R.A. Moyer, T.H. Osborne, M.J. Schaffer, W.P. West, L.W. Yan, J.A. Boedo, E.J. Doyle, G.L. Jackson, I. Joseph, C.J. Lasnier, A.W. Leonard, T.L. Rhodes, P.R. Thomas, J.G. Watkins, and L. Zeng, Phys. Plasmas **13**, 056121 (2006).

[44] H.K. Kim, H.L. Yang, G.H. Kim, J.-Y. Kim, H. Jhang, J.S. Bak, and G.S. Lee, Fusion Eng. Des. **84**, 1029 (2009).

[45] K. Kim, W. Choe, Y. In, W.H. Ko, M.J. Choi, J.G. Bak, H.S. Kim, Y.M. Jeon, J.G. Kwak, S.W. Yoon, Y.K. Oh, and J.-K. Park, Nucl. Fusion **57**, 126035 (2017).

[46] R. Nazikian, D. Eldon, T. Evans, N.M. Ferraro, B.A. Grierson, R.J. Groebner, J.D. King, E. Kolemen, N.C. Logan, G.R. McKee, O. Meneghini, R.A. Moyer, D.M. Orlov, T.H. Osborne, C. Paz-Soldan, C.C. Petty, T.L. Rhodes, W.M. Solomon, O. Schmitz, M.W. Shafer, S.P. Smith, P.B. Snyder, E.J. Strait, and M.R. Wade, 25th IAEA Int. Conf. on Fusion Energy (St Petersburg, Russia, 2014) EX/1-1.

[47] O. Meneghini, P.B. Snyder, S.P. Smith, J. Candy, G.M. Staebler, E.A. Belli, L.L. Lao, J.M. Park, D.L. Green, W. Elwasif, B.A. Grierson, and C. Holland, Phys. Plasmas **23**, 042507 (2016).

[48] J.-K. Park and N.C. Logan, Phys. Plasmas **24**, 032505 (2017).

[49] D.A. Ryan, Y.Q. Liu, L. Li, A. Kirk, M. Dunne, B. Dudson, P. Piovesan, W. Suttrop, M. Willensdorfer, the ASDEX Upgrade team4 and the, ASDEX Upgrade team and the EUROfusion MST team, and and, Plasma Phys. Control. Fusion **59**, 024005 (2017).

[50] J. Breslau, M. Gorelenkova, F. Poli, J. Sachdev, and X. Yuan, *TRANSP V18.2. Computer Software.* (2018).

[51] Q. Yu, S. Günter, and B.D. Scott, Phys. Plasmas **10**, 797 (2003).

[52] Q. Yu, Nucl. Fusion **50**, 025014 (2010).

[53] Q. Yu and S. Günter, Nucl. Fusion **51**, 073030 (2011).

[54] Q. Hu, N.C. Logan, J.-K. Park, C. Paz-Soldan, R. Nazikian, and Q. Yu, Nucl. Fusion **60**, 076006 (2020).

[55] M.W. Jakubowski, O. Schmitz, S.S. Abdullaev, S. Brezinsek, K.H. Finken, A. Krämer-Flecken, M. Lehnen, U. Samm, K.H. Spatschek, B. Unterberg, R.C. Wolf, and TEXTOR team, Phys. Rev. Lett. **96**, 035004 (2006).

[56] F.L. Waelbroeck, I. Joseph, E. Nardon, M. Bécoulet, and R. Fitzpatrick, Nucl. Fusion **52**, 074004 (2012).

[57] S. Günter, Q. Yu, J. Krüger, and K. Lackner, J. Comput. Phys. **209**, 354 (2005).

[58] R. Fitzpatrick, Nucl. Fusion **33**, 1049 (1993).

[59] S. Mordijck, E.J. Doyle, G.R. McKee, R.A. Moyer, T.L. Rhodes, L. Zeng, N. Commaux, M.E. Fenstermacher, K.W. Gentle, H. Reimerdes, O. Schmitz, W.M. Solomon, G.M. Staebler, and G. Wang, Phys. Plasmas **19**, 056503 (2012).

[60] G.R. McKee, Z. Yan, C. Holland, R.J. Buttery, T.E. Evans, R.A. Moyer, S. Mordijck, R. Nazikian, T.L. Rhodes, O. Schmitz, and M.R. Wade, Nucl. Fusion **53**, 113011 (2013).

[61] R. Hager, C.S. Chang, N.M. Ferraro, and R. Nazikian, Nucl. Fusion **59**, 126009 (2019).

[62] R. Hager, C.S. Chang, N.M. Ferraro, and R. Nazikian, Phys. Plasmas **27**, 062301 (2020).

[63] Y.B. Kim, P.H. Diamond, and R.J. Groebner, Phys. Fluids B **3**, 2050 (1991).

[64] C. Paz-Soldan, N.C. Logan, S.R. Haskey, R. Nazikian, E.J. Strait, X. Chen, N.M. Ferraro, J.D. King, B.C. Lyons, and J.-K. Park, Nucl. Fusion **56**, 056001 (2016).

[65] J.D. King, E.J. Strait, R. Nazikian, C. Paz-Soldan, D. Eldon, M.E. Fenstermacher, N.M. Ferraro, J.M. Hanson, S.R. Haskey, R.J. La Haye, M.J. Lanctot, S.A. Lazerson, N.C. Logan, Y.Q. Liu, M. Okabayashi, J.-K. Park, D. Shiraki, and A.D. Turnbull, Phys. Plasmas **22**, 112502 (2015).

[66] Z.R. Wang, M.J. Lanctot, Y.Q. Liu, J.-K. Park, and J.E. Menard, Phys. Rev. Lett. **114**, 145005 (2015).

[67] D. Eldon, B.D. Bray, T.M. Deterly, C. Liu, M. Watkins, R.J. Groebner, A.W. Leonard, T.H. Osborne, P.B. Snyder, R.L. Boivin, and G.R. Tynan, Rev. Sci. Instrum. **83**, 10E343 (2012).

[68] T.H. Osborne, J.R. Ferron, R.J. Groebner, L.L. Lao, A.W. Leonard, M.A. Mahdavi, R. Maingi, R.L. Miller, A.D. Turnbull, M. Wade, and J. Watkins, Plasma Phys. Control. Fusion **42**, A175 (2000).

[69] D.B. Weisberg, C. Paz-Soldan, Y.Q. Liu, and N.C. Logan, Nucl. Fusion **59**, 086060 (2019).

[70] S. Gu, Y. Sun, C. Paz-Soldan, R. Nazikian, M. Jia, H.H. Wang, W. Guo, Y.Q. Liu, T. Abrams, L. Cui, T. Evans, A. Garofalo, X. Gong, N.C. Logan, S. Munaretto, D. Orlov, and T. Shi, Nucl. Fusion **59**, 026012 (2019).

[71] J. Park, A.H. Boozer, and J.E. Menard, Phys. Rev. Lett. **102**, 065002 (2009).

[72] Y. Liu, C. Paz-Soldan, L. Li, and Y. Sun, Nucl. Fusion **60**, 036018 (2020).

[73] N.C. Logan, J.-K. Park, K. Kim, Z. Wang, and J.W. Berkery, Phys. Plasmas **20**, 122507 (2013).

[74] K.C. Shaing, K. Ida, and S.A. Sabbagh, Nucl. Fusion **55**, 125001 (2015).

[75] W. Zhu, S.A. Sabbagh, R.E. Bell, J.M. Bialek, M.G. Bell, B.P. LeBlanc, S.M. Kaye, F.M. Levinton, J.E. Menard, K.C. Shaing, A.C. Sontag, and H. Yuh, Phys. Rev. Lett. **96**, 225002 (2006).

[76] A.M. Garofalo, K.H. Burrell, J.C. DeBoo, J.S. deGrassie, G.L. Jackson, M. Lanctot, H. Reimerdes, M.J. Schaffer, W.M. Solomon, and E.J. Strait, Phys. Rev. Lett. **101**, 195005 (2008).

[77] S.M. Yang, J.-K. Park, Y.-S. Na, Z.R. Wang, W.H. Ko, Y. In, J.H. Lee, K.D. Lee, and S.K. Kim, Phys. Rev. Lett. **123**, 095001 (2019).

[78] R. Nazikian, Q. Hu, A. Ashourvan, D. Eldon, T.E. Evans, B.A. Grierson, N. Logan, D.M. Orlov, J.-K. Park, C. Paz-Soldan, F.M. Poli, and Q. Yu, Nucl. Fusion in press https://doi.org/10.1088/1741 (2021).

[79] R.J. Buttery, S. Gerhardt, R.J.L. Haye, Y.Q. Liu, H. Reimerdes, S. Sabbagh, M.S. Chu, T.H. Osborne, J.-K. Park, R.I. Pinsker, E.J. Strait, and J.H.Y. and, Nucl. Fusion **51**, 073016 (2011).

[80] E.J. Strait, Phys. Plasmas **22**, 021803 (2014).

[81] S.M. Yang, J.-K. Park, N.C. Logan, C. Zhu, Q. Hu, Y.M. Jeon, Y. In, W.H. Ko, S.K. Kim, Y.H. Lee, and Y.S. Na, Nucl. Fusion **60**, 096023 (2020).